Experiments in Fluids (2022) 63:84
https://doi.org/10.1007/s00348-022-03436-3

RESEARCH ARTICLE

Jet noise predictions by time marching of single-snapshot tomographic PIV fields

Daniele Ragni[1] · **Daniele Fiscaletti**[1] · **Woutijn J. Baars**[1]

Received: 14 February 2022 / Revised: 11 April 2022 / Accepted: 12 April 2022 / Published online: 13 May 2022

Abstract

This work combines the latest advancements in time marching of 3D vector fields from tomographic particle image velocimetry, with an adapted version of Lighthill's formulation, for the prediction of far-field jet noise. Three-dimensional velocity vector fields of the jet flow are first reconstructed from a tomographic volume of 4×3×9.5 D_j^3, with $D_j = 5$ cm being the jet-exit diameter. (The jet-exit Mach number M_j ranges from 0.10 to 0.20.) The obtained vector fields are then used as input to a recently developed procedure for the time marching of the vorticity field, which relies upon the vortex-in-cell methodology. This yields time series of each three-dimensional velocity field, from which the far-field pressure is computed via Lilley's acoustic analogy (through evaluation of the Lighthill's stress tensor). It is shown that the estimate of the far-field noise spectrum compares well with the spectrum measured directly from a far-field microphone in the anechoic A-tunnel facility of TU Delft, in the Strouhal number range from approximately 1 to 12.

Graphical Abstract

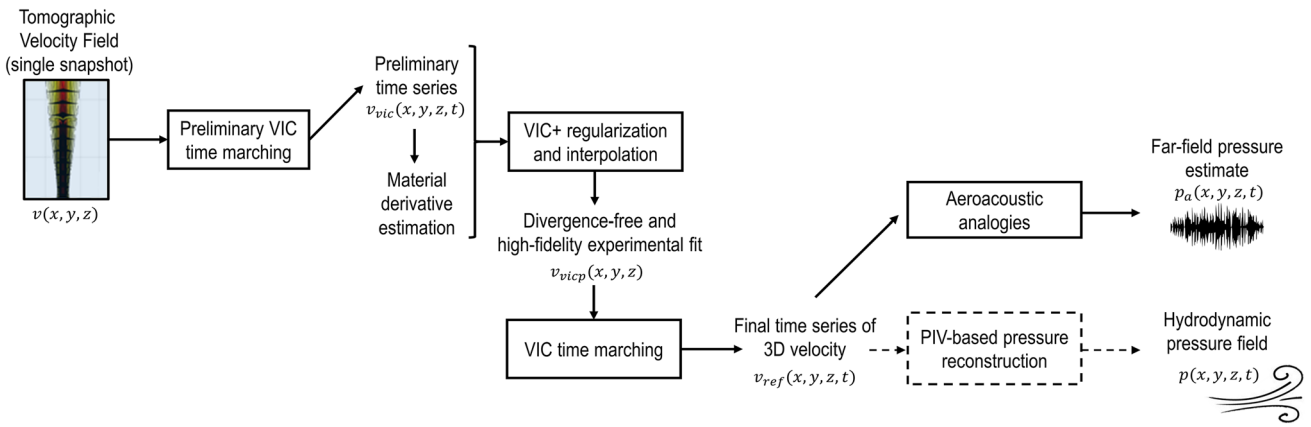

1 Introduction

Turbulent jets are among the most investigated flows in several engineering applications. Whether in a continuous (Crow and Champagne 1971) or pulsatile (Hewitt and Duck 2011) configuration, the local injection of momentum in a quiescent fluid creates a turbulent flow of rare physical complexity (List 1982). In his pioneering schlieren visualizations, Anderson (1956) observed that the near field of a jet is

✉ Daniele Ragni
d.ragni@tudelft.nl

[1] Faculty of Aerospace Engineering, Delft University of Technology, Kluyverweg 1, 2629HS Delft, The Netherlands

organized into vortex rings that form in a region of a few jet diameters downstream of the jet exit. Later, the formation, development, and breakdown of the coherent structures were found to be a central facet in the noise production mechanism of turbulent jets. For predicting the far-field jet noise, acoustic analogies and analytical methods are preferred from the standpoint that they are relatively easy to compute. However, as addressed in the next sections, the fidelity of these methodologies is constrained either by the necessity for accurate and time-resolved flow information as input, or by the robustness of empirical coefficients calibrated through experimental campaigns. To overcome these limitations, the current work presents a robust workflow for performing far-field predictions of jet noise, at relatively high Reynolds number, and solely based on single-snapshot tomographic particle image velocimetry (PIV). In the following section, before discussing the acoustic analogies and the analytical methods commonly applied in the prediction of jet noise, a brief review is presented on the fundamental aspects of coherent structures in jets and their role in the production of noise.

1.1 Coherent flow structures in turbulent jets

By using a planar configuration complementing a laser-induced fluorescence setup for flow visualization, Liepmann and Gharib (1992) were among the first investigators to use PIV to visualize "Bernal–Roshko"-type (Bernal and Roshko 1986) structures, by computing the streamwise vorticity in the jet's shear layer. Such structures were responsible for the entrainment process in the near vicinity of the jet exit and consequently for an increase in the length scale of the flow structures along the axial direction (Hussain 1986; Liepmann and Gharib 1992; Jordan et al. 2007; Yule 1978). Citriniti and George (2000) applied proper orthogonal decomposition (POD) to cross planes of the instantaneous streamwise velocities, which were obtained from an array of 138 hot-wire anemometer probes in a jet mixing layer. Their study supported the conclusions of Liepmann and Gharib (1992), in that the growth of shear-layer instabilities was linked to the jet flow entrainment. Earlier on, it was already conjectured that the alteration of coherent flow structures in the entrainment region of the jet contributes to the noise production (Goldstein 1976). In the context of an axially extended jet noise source, it is known that the region most active in the noise production resides where the potential core of the jet flow collapses. Both upstream and downstream of this region, where the shear-layer instability waves grow and decay in strength, respectively (Suponitsky et al. 2010; Sandham et al. 2006), their convection velocities strongly depend on the radial location. In particular, in the outer entrainment regions of the shear layer, the convection of the structures is faster than the mean flow, while it is slower than the latter close to the jet centerline (Ko and Davies 1971; Kerhervé et al. 2004). Several works have also investigated the azimuthal organization of the turbulent structures (Glauser and George 1987; Citriniti and George 2000; Iqbal and Thomas 2007; Tinney et al. 2008), concluding that the high-speed regions near the jet centerline comprise most energy in the low azimuthal mode-numbers (e.g., the breathing and helical mode), while the outside regions are governed by higher azimuthal mode structures. Commendable efforts have been directed to the understanding of relationship between the dominant structural modes in the flow. For example, works utilizing POD (Glauser and George 1987; Citriniti and George 2000; Jung et al. 2004; Tinney et al. 2008; Lasagna et al. 2021) revealed that "volcano-like" and short-duration eruptions of high-strain turbulent flow co-exist with the streamwise vortices and that they are most intense after the collapse of the potential core. Other works have also confirmed through correlation-based techniques that the shear layer comprises long streaky structures and series of toroidal shear-layer vortices in the outer regions of the jet (Iqbal and Thomas 2007; Nogueira et al. 2019; Samie et al. 2021).

In summary, the jet noise source field comprises a multitude of spatial length scales that axially and radially evolve in time. Isolating the turbulence that solely contributes to the noise production requires a methodology able to capture an extended region of the three-dimensional (3D) jet flow and to link the development of the flow structures to the acoustic pressure in the far field. The full jet development region that is relevant for the noise production mechanism can extend up to $20D_j$ in the axial direction. However, the strongest mean flow deceleration region, just aft of the potential core, is the most intense contributor to the noise (Bogey and Bailly 2007; Tinney et al. 2008) and is typically confined to within $x = 5D_j$ to $10D_j$ (Kyle and Sreenivasan 1993; Bastin et al. 1997; Guj et al. 2003; Kerhervé et al. 2012).

1.2 Noise emitted by coherent flow structures

The far-field noise of a jet is dictated by the organization and intensity of the flow structures in its near field. Over the past two decades, this has been evidenced by a reasonably successful approach that models the coherent flow structures as traveling wave-packets (Morris 2009; Papamoschou 2011; Jordan and Colonius 2013). Their key role in the production of noise has unequivocally been proved in the recent numerical study of Fu et al. (2017). For example, the pressure wave-packet characteristics can be inferred by measuring the pressure fluctuations in the acoustic near field with arrays of microphones (i.e., Breaky et al. 2017). Additionally, array of microphones can be used to map the spatial topography of the sound pressure of the jet along the emission path, as demonstrated by Baars et al. (2021). However, capturing the

hydrodynamic velocity and pressure fields with sufficient spatial dynamic range is very challenging, especially when needed to tune or validate analytical methods for far-field noise prediction. This is why the number of research efforts on the acquisition of the 3D velocity and pressure fields is rather limited. Matsuda and Sakakibara (2005) advanced the reconstruction of 3D flow structures from stereoscopic PIV measurements by relying on Taylor's hypothesis of "frozen turbulence" (Taylor 1938), to temporally evolve instantaneous, stereoscopic velocity fields acquired perpendicular to the jet axis. Other studies employed two synchronized, either time-resolved stereo PIV systems (Jaunet et al. 2017), or in a dual-time configuration (Pinier and Glauser 2017), to infer the structure of the coherent flow structures and wavepackets. The advent of time-resolved tomographic PIV (Elsinga et al. 2006) made possible to focus on specific regions of the jet flow. Violato and Scarano (2011) resolved the jet's transitional region and identified the pairing of azimuthal vortex rings as the main contributor to the overall noise production. One of the common limitations of volumetric laser illumination techniques is the measurement domain size (Scarano 2012), which, in the work of Violato and Scarano (2011) (working in water with larger scattering particles) only allowed for a view on the early onset of the fully 3D shear-layer instabilities, thus excluding any noise-producing mechanisms associated with the collapse of the potential core.

1.3 The role of acoustic analogies in jet noise

Aeroacoustic analogies enable to solve the far-field pressure using source terms from an unsteady flow. In particular, the evaluation of the two-point cross-correlation function of Lighthill's turbulent stress tensor (Lighthill 1954) is directly related to the spectral density of the far-field noise (Morris and Farassat 2002). For flows with mean shear, Lilley's analogy supports the so-called flow-acoustic interactions (Lilley 1974; Colonius et al. 1997). In fact, the spectral decay of the far-field noise beyond the Strouhal number corresponding to the peak intensity is correlated with the turbulence decay and thus with the jet development characteristics. High-speed applications of volumetric velocimetry measurements can capture the required source terms as long as the acoustic analogies can be applied using measurable quantities as input (Morris and Farassat 2002). Various works have shown promise in using acoustic analogies with experimental input data for jet noise predictions. Seiner et al. (1999) characterized the noise sources of a jet with exit Mach equal to 0.85 using two-point turbulence statistics. In a subsonic (and acoustically excited) jet at low Reynolds number, Schram and Hirschberg (2003) (and later Schram et al. (2005)) opted for the use of a conservative form of the vortex-sound theory. This allowed them to match an analytical noise prediction on phase-locked planar PIV, with a direct microphone measurement. Although promising, the use of formulations based on the integration of the velocity field, or the second time-derivative of the Lamb vector, requires a careful optimization of the PIV setup, e.g., see Violato and Scarano (2011) for a comparison between the aeroacoustic sources and the flow structures obtained with the $\lambda 2$-criterion (Jeong and Hussain 1995). The main caveat in applying an experimental measurement technique is again related to limitations on the extent of the measurement domain, provided that a sufficient spatial and temporal resolution is obtained to achieve meaningful acoustic predictions. To the contrary, high-fidelity numerical data of jet turbulence overcome the inherent limitations associated with both domain size and resolution aspects (Freund 2001; Bogey et al. 2003). In this respect, several authors have opted for inviscid vortex dynamics simulations (Martin and Meiburg 1991) or lately for lattice Boltzmann solvers (Lew and Mongeau 2010). However, although numerical approaches have advantages in terms of spatially and temporally resolved source terms, an inherent shortcoming is the maximum achievable Reynolds number due to computational expenses (Kaushik and Kumar 2015). Regardless, several unsteady jet flow phenomena are strongly dependent on the Reynolds number because they are either governed by the location of the transitional regime or the range of scales in the jet development region. An example of the latter is the axis-switching phenomenon of the vortical flow structures (Suzuki 2010), which depends on the jet density and temperature ratios, and thus Re_{D_j} (Crow and Champagne 1971; Mankbadi and Liu 1984; Cavalieri et al. 2012).

1.4 Contribution and overview

A new framework is introduced, based on the post-processing technique of Schneiders et al. (2014) to yield the source terms in turbulent jet flows from single-snapshot tomographic vector fields. The approach relies on a revised version of Lighthill's acoustic analogy, and it is capable of estimating the far-field noise spectrum in a range of Strouhal numbers where analytical methods typically rely on experimental calibration (Morris and Farassat 2002). The time-marching aspect of the single tomographic volumes further allows breaking through conventional limitations of high-speed lasers for jet flows at high Reynolds number.

The paper is structured as follows. Section 2 presents the experimental setup, while Sect. 3 covers the validation of the jet flow statistics. Section 4 presents the data post-processing steps to obtain the far-field pressure from a single 3D vector field. In Sect. 5, the time-marching algorithm and its output are covered. This is followed by estimates of far-field noise spectra in Sect. 6 and by the conclusions in Sect. 7.

2 Experimental setup

The experimental study was conducted in the anechoic tunnel (A-tunnel) of the low-speed laboratories of the Faculty of Aerospace Engineering, at Delft University of Technology. Full details of this vertical wind-tunnel facility are described in Merino-Martinez et al. (2020). The A-tunnel contraction enters the testing room as a circular, 60 cm diameter, section. For the current jet flow investigations, a new large-scale contraction was printed with additive manufacturing, which smoothly contracted the inlet flow into a circular jet nozzle with an exit diameter of $D_j = 5$ cm. A third-order polynomial describes the profile of the axisymmetric jet-nozzle contraction until it reaches a diameter of 10 cm. Downstream of the latter, the exit jet consists of a conical section angled at 4.7°. Schematic illustrations of the facility and of the jet-nozzle contraction are presented in Fig. 1. Three jet-exit velocities are tested in this study: $v_j = [34\ \mathrm{ms}^{-1}, 51\ \mathrm{ms}^{-1}, 68\ \mathrm{ms}^{-1}]$, corresponding to jet-exit Mach numbers of $M_j = [0.1, 0.15, 0.2]$ and to Reynolds numbers of $\mathrm{Re}_{D_j} = [1.2{\times}10^5, 2.4{\times}10^5, 3.6{\times}10^5]$, respectively. A detailed assessment of the jet flow is performed using hot-wire anemometry, double-plane stereoscopic PIV and tomographic PIV. While a statistical characterization of the jet mean flow field (for validation purposes, see Sect. 3) is considered in the mid-plane of the jet using hot-wire anemometry and stereoscopic PIV, the tomographic PIV data are used as input for the far-field noise prediction methodology (Sect. 5 and beyond). For brevity, the noise estimation procedure is only illustrated for $M_j = 0.15$.

2.1 Double stereoscopic PIV

Two stereoscopic PIV setups were employed and combined to obtain a single vector field capturing the full axial jet flow evolution. Both stereoscopic PIV setups feature two LaVision Imager sCMOS CLHS cameras (4 Mpx, $2560 \times 2160\ \mathrm{px}^2$, 16 bit, 6.5 µm/px), installed at an angle of about 75 deg in the azimuthal plane of the jet. Illumination was provided by a dual-pulsed Nd:Yag EverGreen laser with a 200 mJ per pulse energy at 15 Hz. Optics conveyed the laser light to a laser sheet of about 2 mm thickness. Four Nikkor AF-S lenses with 60 mm focal length at an aperture $f\# = 11$ were placed at about 1.2 m distance together with four Scheimpflug adaptors, to obtain two consecutive planar fields of view each covering approximately 260 mm in the axial direction. This resulted in a combined field of 520 mm ($\approx 10.5 D_j$). The single fields were imaged at about 9.8 px mm^1 resolution and with a magnification factor of 0.06. A total amount of 1000 image pairs were recorded per free-stream velocity at an acquisition frequency of 10 Hz. The recordings were evaluated with the LaVision DaVis 10.1 software, featuring a window deformation iterative multi-grid approach (Scarano and Riethmuller 1999) with a window size of $8{\times}8\ \mathrm{px}^2$ at 75% overlap (leaving a final vector resolution of 0.8 mm and a vector spacing of 0.2 mm). A schematic representation of the stereoscopic PIV setup is

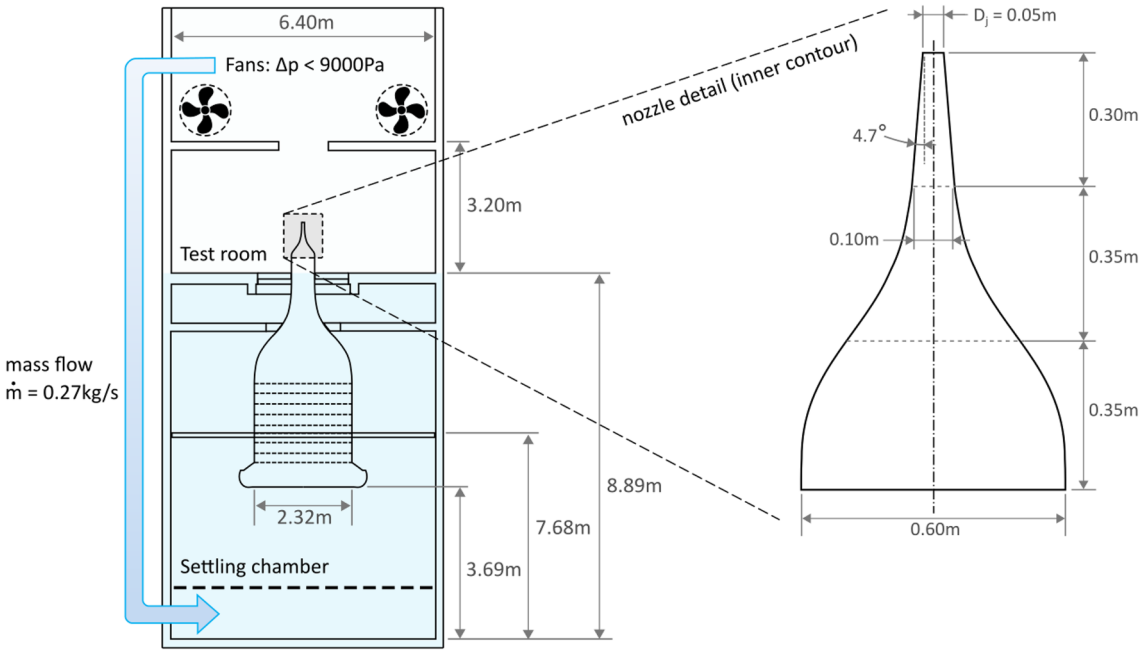

Fig. 1 Schematic of (left) the A-tunnel facility and (right) the inner contour of the jet nozzle, produced with additive manufacturing

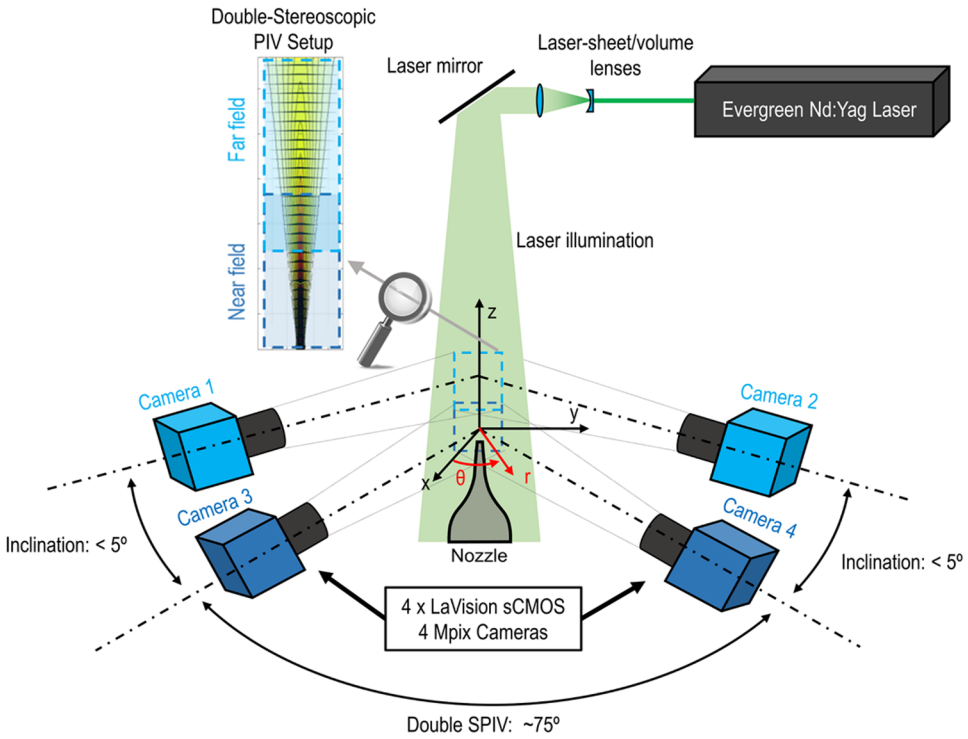

Fig. 2 Schematic of the double stereoscopic PIV setup

presented in Fig. 2. The main sources of uncertainty in the stereoscopic PIV fields are caused by peak locking, finite spatial resolution, stereoscopic calibration and cross-correlation (Raffel et al. 2007). Errors due to peak locking are quantified by comparing the size of the imaged particles with their actual size on the sensor. With a digital resolution of 9.8 px/mm, a magnification factor of 0.06 and a diaphragm aperture of $f\# = 11$, the in-focus imaged particle on the sensor is of 18 µm (Adrian and Yao 1985), which corresponds to about 2.7 px. This allows obtaining a stochastic distribution of round-off errors in the computed velocity field, avoiding problems of peak locking (Westerweel 1997). The procedure is additionally verified by analysis of the histogram of the round-off value of the particle vector displacements. Errors due to modulation by finite spatial resolution of the resulting velocity fields are also influencing the measured flow structures. With the multi-pass cross-correlation algorithm featuring window deformation (Scarano and Riethmuller 1999), the length scale of flow structures measured with less than 5% modulation needs to be larger than 1.7 times the window size (Schrijer and Scarano 2014). Having a window size of 8×8 px^2 corresponding to 0.8 mm resolution in the entire field, flow structures down to 1.36 mm can be measured with 95% accuracy. Errors due to stereoscopic calibration are mitigated by an iterative self-calibration procedure (Raffel et al. 2007), applied to further improve the fitting of the warped images from the position of the calibration target to the position of the laser sheet. By employment of a polynomial mapping that combines the images into the self-calibrated stereoscopic plane above in LaVision DaVis 10.1, the residual errors due to self-calibration are finally assessed to account for less than 0.05 px, which is considered satisfactory to process the results with the stereo cross-correlation algorithm (Raffel et al. 2007). Random errors are mainly due to the cross-correlation algorithm. In the present study, due to the large dynamic range of vector displacements within the jet and outside the shear layer, errors were found to vary with respect to the region of interest. With 1000 uncorrelated samples per test case, errors on the instantaneous fields amount to less than 1% of v_j at the jet exit and less than 5% of v_j in the outer part of the jet shear layer. Quantification of the overall level of uncertainty, when considering the size of the statistical sample, asses the final uncertainty on the mean velocity to 0.05% of the jet-exit velocity and on the root mean square to 3% of the maximum fluctuations in the outer part of the shear layer. The method used to estimate the previous values is validated with the work of Wieneke (2015).

2.2 Tomographic PIV

A tomographic PIV setup featured the same four cameras as used in the double stereoscopic PIV setup, but mounted at the four vertices of a pyramid with 30 deg angle with respect to the jet axis (Fig 3—left). The positioning of the cameras was in forward scattering with respect to the laser beam. The particular choice of the very far positioning of the laser downstream of the jet gave beneficial

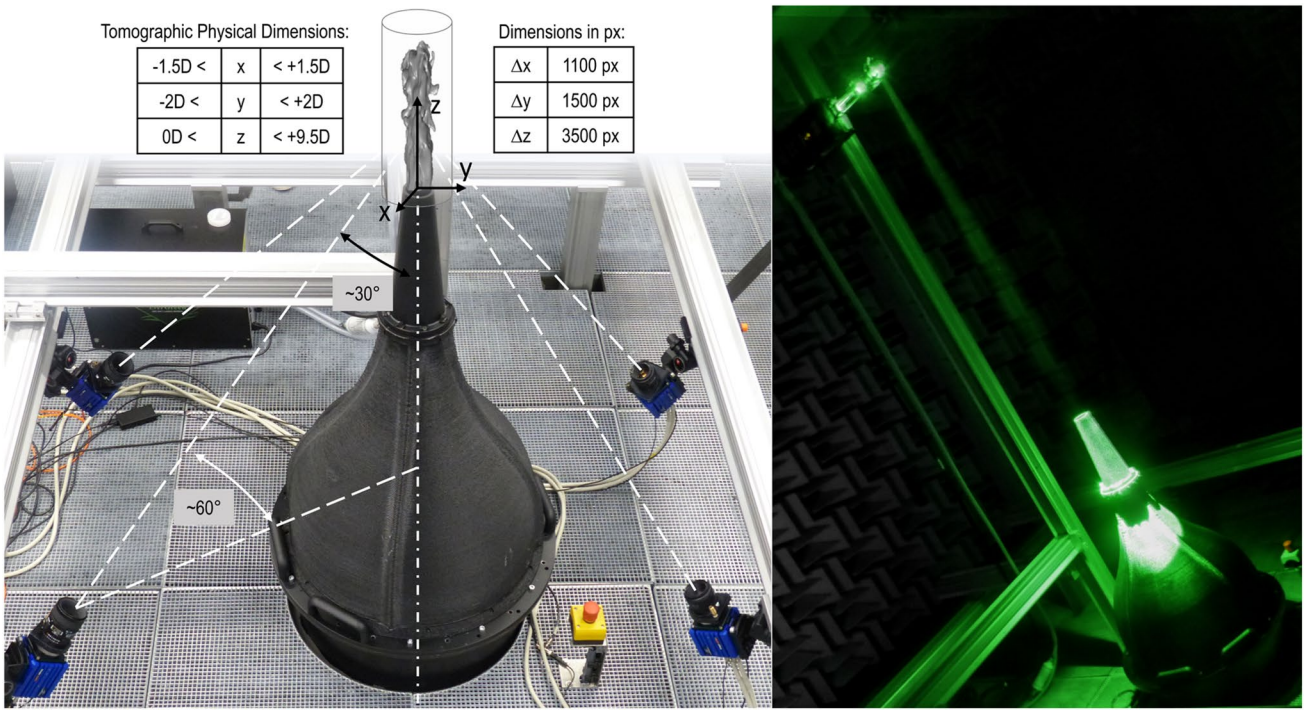

Fig. 3 Photographs of the tomographic PIV setup, showing (left) the positioning of the cameras and the dimensions of the measurement volume, and (right) the conical laser beam

advantages on the amount of scattered light collected from the particles, especially when compared with backward scattering configurations (Elsinga et al. 2006). The correlation volume spanned $[\Delta x, \Delta y, \Delta z] \approx [3D_j, 4D_j, 9.5D_j]$. A photograph of the camera arrangement together with the laser illumination is presented in Fig. 3. To obtain a sufficiently large depth of field in the measurement volume, the diaphragm of the cameras was reduced (i.e., $f\#$ brought to 22). The double-cavity Nd:Yag EverGreen laser was further expanded to form a slowly diverging conical volume that illuminated the near field of the jet flow. The tomographic reconstruction of the single snapshots was performed with the fast multiplicative algebraic reconstruction technique (FastMART) in LaVision DaVis 10.1 (Herman and Lent 1976). A volume of approximately 1100×1500×3500 px^3 with a digital resolution of 7.5 px/mm was generated and subsequently processed with a fast Fourier transform algorithm with a window size of $48 \times 48 \times 64$ px^3. A post-processing step with a universal outlier detection (Westerweel 1994) was applied to the 3D vector fields to isolate and replace any outlier vector resulting from loss of correlations that could be attributed to a non-uniform particle concentration. Data were additionally interpolated onto a uniform grid with a vector spacing of 0.5 mm for visualization. Uncertainties in the velocity time series and the pressure fields as obtained from the finite time marching of the VIC methodology are dependent on the uncertainty of the vector fields. Due to the reduced magnification factor of 0.06 corresponding to a lower digital resolution of about 7.5 px/mm, errors due to modulation by finite spatial resolution of the resulting velocity fields are higher with respect to the stereoscopic setups (i.e., flow structures with about 2 mm can be measured with 95% accuracy). The uncertainties propagate in the time marching and in the material derivative computation (see Sect. 4). The main systematic error in the time series of the velocity fields is dependent on the flow acceleration between the subsequent multiple vector fields and, following the work of Boillot and Prasad (1996), it reads:

$$\epsilon_{u,\mathrm{sys}} = \frac{1}{4}\Delta t^2 \left| \frac{D\boldsymbol{v}}{Dt} \right| \tag{1}$$

where $\frac{D\boldsymbol{v}}{Dt}$ is the material acceleration obtained from the finite time marching. The separation time for the computation is derived from the Courant–Friedrichs–Lewy (CFL) (Courant et al. 1928) condition with the spatial resolution of the tomographic setup. From analysis of the time series, more than 90% of the data possessed a material acceleration below 15 km s^{-2}. Based on Eq. (1), the systematic error in the velocity fields is estimated to be about 1.5 µm (0.01 px). The final formula of the error on the pressure fluctuations as obtained from the material acceleration with the Lagrangian method is associated with two sources, i.e., the first source

due to the truncation of the derivative and the second source due to random components on the velocity fields (cfr. study of Violato et al. (2011)):

$$\epsilon_p \approx \rho h_{\text{res}} \left[\frac{1}{2}(n\Delta t)^2 \left| \frac{D\boldsymbol{v}}{Dt} \right| \cdot \frac{|\nabla \cdot \boldsymbol{v}|}{\Delta t} + \frac{\epsilon_V}{2n\Delta t} \right] \tag{2}$$

where h_{res} is the actual vector spacing along the particle trajectory and n is the stencil of the $2n + 1$ vector fields used for the material-derivative computation. In this study, it is assumed that the Poisson integration does not add significant errors to the pressure evaluation (de Kat and van Oudheusden 2012). Substituting in Eq. (2) all values, the total error on the pressure fluctuations is about 10 Pa. If this error had totally to be ascribed to an uncertainty on the velocity fluctuations, by following the eighth power rule that would correspond to less than 1 dB in the noise spectra.

2.3 Acoustic measurements

Acoustic far-field data were acquired in the anechoic facility for validation purposes. Measurements of the acoustic pressure time series were performed with a G.R.A.S. 46BE free-field microphone, comprising a precision of ± 2 dB within a frequency range of 4 Hz to 80 kHz. The microphone's dynamic range spans from 35 dB up to 160 dB, with a reference pressure of 20 μPa. With the polar angle adhering to the convention of $\theta = 0$ deg being the upstream direction of the jet axis, the microphone was positioned at $\theta = 90$ deg and was mounted in the nozzle exit plane, at a radial distance of 1 m, equivalent to $r = 20D_j$. Although at this radiation angle the acoustic pressure of the jet noise is not the strongest, the present measurement location corresponds to the most accurate positioning of the microphone with the aim to demonstrate the methodology. In particular, the relative positioning of the microphone with respect to the jet was carried out with the laser alignment device GeoFennel FL 55 PLUS HP, which determined a final alignment accuracy of about 0.1 deg with respect to the different elements of the setup. The measurements were performed with a sampling frequency of 51.2 kHz for a duration of 30 s. For post-processing, the acoustic data were split into blocks of 2048 samples for each Fourier transform, and windowed with a Hanning weighting function with 50% overlap. These parameters result in a spectral resolution of 25 Hz.

2.4 Hot wire anemometry

A single-sensor miniature wire probe model 55P15 from Dantec Dynamics was employed in this study. The sensitive wire was made of platinum-plated tungsten having a length of 1.25 mm and a diameter of 5 µm. The probe was positioned at streamwise positions that are multiple integers of the jet diameter. The probe was traversed through a Zaber LRQ150HL–DE51T3 traverse controller with 0.15 µm accuracy. Conditioning of the sensor was carried out with a TSI IFA–300 CTA module, and acquisition was performed with National Instruments NI–9234 cards (± 5 V, 24 bit resolution). For each acquisition point, the signal was acquired for 12 s using the sampling frequency of 51.2 kHz. The calibration used a fourth-order polynomial curve fitting of the output voltages (Bruun 1995) with data from 17 speed–voltage data points with logarithmic spacing between the lowest and the highest free-stream flow speed v_j. The reference velocity information was taken from a Pitot tube installed near the hot-wire probe.

3 Turbulent jet flow statistics

Figure 4 shows the mean (left column) and fluctuating (right column) velocity fields for the case of $M_j = 0.15$. The velocity fields are presented in terms of the jet cylindrical components, i.e., streamwise (or axial) v_z, radial v_r and azimuthal v_θ components, normalized with the jet-exit velocity v_j. The potential core of the jet, defined as the region where $v_z/v_j > 0.9$, extends up to $z/D_j \approx 4$. From this region, the shear layer spreads with an angle of approximately 4°, as estimated from the mean flow field. These findings are consistent with what is reported by Iqbal and Thomas (2007). The mean velocity field develops mostly in the axial direction, with both radial and azimuthal velocity components reaching maxima of about 1% of v_j in proximity of the nozzle exit. From the radial velocity contours, a very small component in the direction of the jet axis from the surrounding fluid is measured, showing traces of entrainment from the outside flow, while the shear layer pushes outward allowing for a positive jet spreading rate from the inside. A drastic increase in the turbulence energy within the jet is measured at the potential-core breakdown, as reported from the literature (Hussain 1986; Jordan et al. 2007), while negligible fluctuations are measured within the potential core (below 0.5%), for all velocity components. Velocity fluctuations raise up to about 15% in the shear-layer region. Starting from a 6-diameter distance from the nozzle exit, the maximum flow fluctuations rapidly decay down to about 8 to 10%. The streamwise velocity component along the jet's centerline is shown in Fig. 5—left. For $z/D_j > 4$, the mean streamwise velocity at the centerline begins to decay, fitting the mass-flow decay model from Hussein et al. (1994) from $z/D_j > 7$, until reaching $v_z/v_j \approx 0.65$ at $z/D_j = 10$.

Figure 5—right presents the velocity fluctuations along the centerline for the three velocity components. The fluctuations of the axial component of the velocity are the strongest, with maxima rapidly building up to 15% at about $z/D_j > 7$ (cfr. Fig. 4—left). Starting from the nozzle exit, the

velocity fluctuations of all components increase until reaching a peak at $z/D_j \approx 7$. The peak of the fluctuations corresponds to the onset of the mixing region. The starting point of the aforementioned mixing region is typically referred to as an alternative definition of the potential core end (Aleyasin et al. 2017), due to transition and entrainment of the

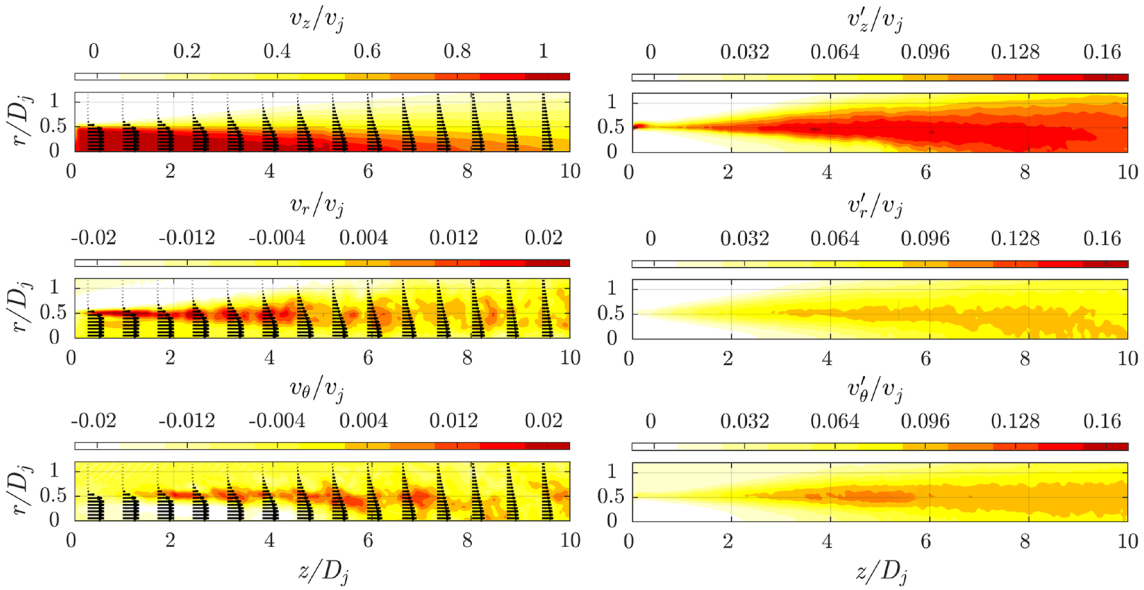

Fig. 4 (left column) Contours of axial v_z, radial v_r and azimuthal v_θ velocity components and (right column) their root-mean-square velocity fluctuations, for the case of $M_j = 0.15$

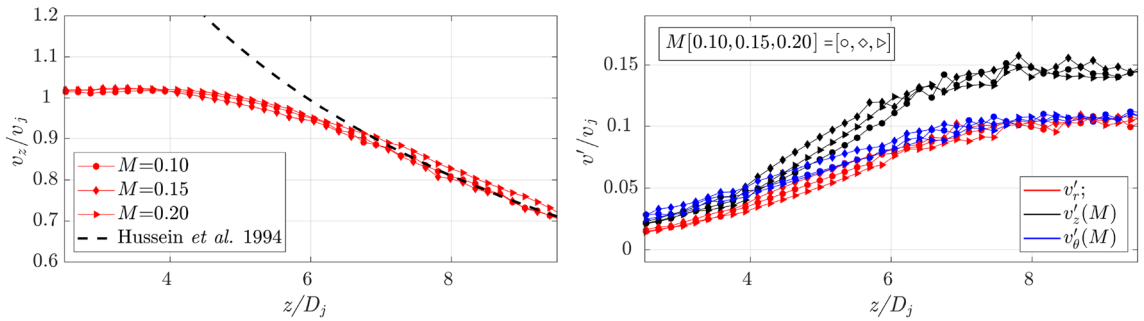

Fig. 6 Similar to Fig. 5, but now for all three jet-exit Mach numbers of $M_j = [0.1,\ 0.15,\ 0.2]$. Comparison of (left) the mean streamwise velocity and (right) the velocity fluctuations along the jet centerline

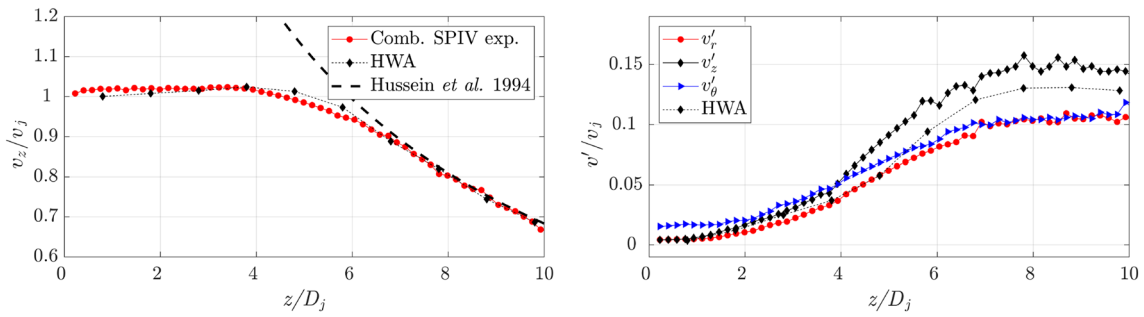

Fig. 5 (left) Streamwise velocity along the jet centerline for $M_j = 0.15$; superimposed is the centerline velocity decay trend from Hussein et al. (1994). (right) Velocity fluctuations of all three components: axial v'_z, radial v'_r, and azimuthal v'_θ; 10-vector skip for visualization

external flow field. Figure 6 presents a final verification of the collapse of the different jet velocity and fluctuations distributions for the three tested Mach numbers in this study. In order to amplify the differences between the datasets, the streamwise region is shortened from $10D_j$ to about $6D_j$. Nevertheless, the measured profiles show very small differences within the different Mach numbers. The minor shift with respect to the fit employed from Fig. 5 is ascribed to uncertainties in the precise estimation of the potential-core start, corresponding to relatively higher velocities.

So far, the discussion of the velocity field was based on the stereoscopic PIV results; the mean velocity profile and mean velocity fluctuations as obtained from tomographic PIV are now considered alongside. A filtering effect on the energy content of the velocity fluctuations is expected from the lower spatial resolution of the tomographic setup and from the 3D cross-correlation procedure (Elsinga et al. 2006). Figure 7 shows the comparison of the statistics from tomographic PIV and from stereoscopic PIV, showing a good agreement in both the decay of the axial velocity component and in the increase in the velocity fluctuations in the cylindrical reference system. A filtering effect in the maximum fluctuations as measured from the tomographic setup is observed and is very much consistent across the different velocity components and accounting for approximately 30% of the same quantity as calculated from stereoscopic PIV.

4 Post-processing methodology

This section describes the workflow for predicting far-field acoustic pressure spectra from only tomographic PIV fields as input.

4.1 Vortex-in-cell technique

The vortex-in-cell (VIC) technique (Schneiders et al. 2014) was used to generate a first time series of velocity fields, with a time-marching procedure applied to the instantaneous tomographic vector fields obtained from the PIV measurements. The methodology was originally developed by Christiansen (1973), and it is based upon the vorticity $\boldsymbol{\omega}$ transport equation:

$$\frac{\partial \boldsymbol{\omega}}{\partial t} + (\boldsymbol{v} \cdot \nabla)\boldsymbol{\omega} = (\boldsymbol{\omega} \cdot \nabla)\boldsymbol{v} + \frac{\mu}{\rho}\nabla^2\boldsymbol{\omega} \tag{3}$$

where $\boldsymbol{v}$ denotes the flow velocity and μ and ρ are the dynamic viscosity and flow density, respectively. It was confirmed that the contribution of the viscous stresses is negligible in this work, due to the relatively higher contribution of the inertial components in the jet, and they are therefore omitted in the remainder of this work. After the 3D vector fields were obtained through the LaVision DaVis 10.1 FastMART algorithm (Sect. 2.2), an additional preprocessing step was applied before running the VIC algorithm. This involved imposing a divergence-free condition in the tomographic velocity field (Schneiders et al. 2014). The divergence-free condition was calculated as a solution of the Poisson equation for the velocity vector $\boldsymbol{v}$ as function of the vorticity field $\boldsymbol{\omega}$ on the Cartesian grid, with the boundary conditions on the domain boundary, $\partial\Omega$, from the originally measured velocity vector $\boldsymbol{v}_{\text{meas}}$:

$$\nabla^2\boldsymbol{v} = -\nabla \times \boldsymbol{\omega}; \quad \boldsymbol{v}|_{\partial\Omega} = \boldsymbol{v}_{\text{meas}}. \tag{4}$$

In the next step, the vorticity field is discretized into a series of Lagrangian particles $\boldsymbol{x}^p$ with index $p = \{1, .., N\}$ and strength $\boldsymbol{\alpha}^p$. The fluid particles are then advected from their original position to the next one in a finite time step. Hereby, the algorithm first displaces the fluid particles from the experimental grid points to new locations by advecting the instantaneous vector fields in time (Scarano and Moore 2012). The particle strength is subsequently computed by applying a vortex-stretching model (Koumoutsakos 2005), from which a new vorticity field is obtained at the grid nodes. Briefly, the two differential equations governing the time marching are:

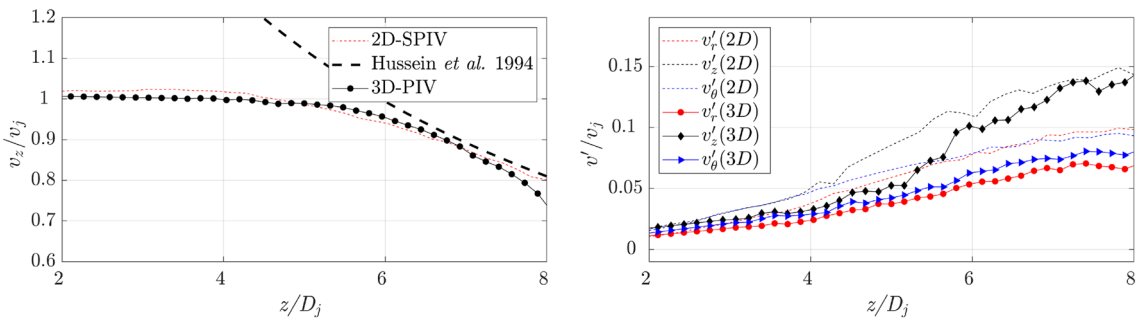

Fig. 7 Comparison between the stereoscopic (denoted as 2D) and tomographic (3D) PIV results, with (left) the streamwise velocity along the jet centerline and (right) the velocity fluctuations of all three components: axial v_z', radial v_r', and azimuthal v_θ'

$$\frac{\partial \boldsymbol{x}^p}{\partial t} = \boldsymbol{v}(\boldsymbol{x}^p, t); \tag{5}$$

$$\frac{\partial \boldsymbol{\alpha}^p}{\partial t} = \boldsymbol{\alpha}^p \cdot \nabla \boldsymbol{v}(\boldsymbol{x}^p, t). \tag{6}$$

It has to be noted that the approach followed in this manuscript differs from the one of Schneiders et al. (2014), since the location and strength of the particles are updated by using the velocity field from the previous time instant (i.e., explicit time-marching formulation). Therefore, it is of paramount importance to provide the algorithm with an accurate input, in order not introduce inaccuracies that could lead to instabilities in the time marching. Additionally, the method computes the evolution of the flow field by propagating the vector solution from the previous time steps, which is derived from the convection of the flow features. A final step is carried out to calculate the new velocity field in time by solving a similar Poisson equation as in Eq. (4), with the advected vorticity as input, and Neumann boundary conditions having null-gradient in the far field.

4.2 Computation of the hydrodynamic pressure

The time-marching algorithm enables the computation of both the velocity material derivative and the pressure gradient, from which the hydrodynamic pressure can be integrated. The material derivative of the flow velocity is obtained from the time series of velocity fields as resulting from the VIC methodology. It has to be noted that the local hydrodynamic pressure fluctuations should not be confused with the far-field acoustic ones. In this paper, the pressure reconstruction methodology is obtained from the material derivative of the flow velocity and completely decoupled from the evaluation of the far-field acoustic pressure, obtained with Lighthill's acoustic analogy. In particular, when considering a stationary orthonormal Cartesian frame of axis and the respective velocity vector $\boldsymbol{v}$, the flow pressure gradient reads:

$$\frac{\nabla p}{\rho} = -\frac{D\boldsymbol{v}}{Dt} + \mu \nabla^2 \boldsymbol{v} \tag{7}$$

where p, ρ and μ are, respectively, the flow pressure, density and dynamic viscosity and the ∂ and D operators represent the partial and material (or total) flow derivatives, respectively. The material derivative of the velocity is estimated using a least-squares fit of the velocities along a reconstructed particle trajectory in a similar way as in Pröbsting et al. (2013). The main changes with respect to the latter are of two types. Firstly, for evaluation of the material derivative in time, a time-stencil corresponding to $n = 2$ is employed, i.e., $\pm$ 2 vector fields with respect to the reference one and therefore $2n+1$ vector fields. Secondly, a Lagrangian fit of the vector field is applied to finally compute the material-derivative coefficients, with a polynomial of order $m = 2$, i.e., a second-order approximation of the flow curvature. The flow pressure is obtained by means of a Poisson solver that integrates the pressure gradient computed from the Navier–Stokes momentum equation using the PIV velocity fields as input. The methodology is well known in the literature, and it has been referenced in several works (Charonko et al. 2010; Ragni et al. 2009; van Oudheusden 2013). Boundary conditions are set by computing the normal components of the pressure gradient and used as Neumann boundary conditions in the streamwise evolution of the jet. Dirichlet-type boundary conditions are applied in the outer part of the jet domain.

4.3 Lighthill's analogy in turbulence-based stationary and moving reference

For the computation of the far-field jet noise, the formulations presented by Goldstein (1976) and Lilley (1974) originally developed from Lighthill's analogy (Lighthill 1952, 1954) are adopted, with the VIC time series as input. As presented by Morris and Farassat (2002), jet noise prediction methods from aeroacoustic analogies enable to considerably lower the costs associated with high-fidelity simulations of the fine-scale turbulence of jet flows. However, as presented by the authors, the reliability of the radiated noise estimate from analytical data or from Reynolds-averaged Navier–Stokes simulations is based upon an accurate prediction of the turbulent flow, especially at the small scales. In particular, it is necessary to approximate the two-point cross-correlation of the turbulent sources, which can be expressed on a frame of reference either stationary or moving with the local mean flow. The acoustic pressure fluctuations in the far field can be written as:

$$p'(\boldsymbol{x}, t) = \frac{1}{4\pi c_0^2 |\boldsymbol{x} - \boldsymbol{y}|} \int_{V_y} \frac{\partial^2}{\partial t^2} T_{xx}\left(\boldsymbol{y}, t - \frac{|\boldsymbol{x} - \boldsymbol{y}|}{c_0}\right) d\boldsymbol{y}. \tag{8}$$

In Eq. (8), the frame of reference at the listener position is indicated with $\boldsymbol{x}$, while the one at the source location is indicated with $\boldsymbol{y}$ (t.b.n. for the volumes we drop the bold notation for the coordinate reference, e.g., V_y). The speed of sound is indicated with c_0, and T_{xx} is the most relevant far-field observer component (t.b.n. in the jet-axis direction) of the Lighthill's stress tensor, in more general form written as:

$$T_{ij} = \rho u_i u_j + \left(p' - \rho' c^2\right)\delta_{ij} - \tau_{ij} \tag{9}$$

where $\rho u_i u_j$ are the local Reynolds stresses of the flow, $p' - \rho c^2$ is the homentropic term difference between the local pressure fluctuations (t.b.n. not to be confused with the ones in Eq. 8) and the ones due to changes in density, δ_{ij} is the Dirac function (i.e., equal to 1 when $i = j$ and equal

to 0 otherwise), and τ_{ij} is the viscous stress tensor. It has to be noted that although the formulation used in Eq. (8) is already simplified to account for the largest contribution of the Lighthill stress tensor, the availability of the experimental data with the present methodology allows extending the formulation with all tensor components. In the present study, considering that the viscous stresses can be neglected and that the dataset pertaining to the chosen Mach numbers determines departures from the isentropic behavior, Eq. (9) can be simplified as $T_{ij} = \rho u_i u_j$, and its expression obtained from the time series of the vector fields, by computing the mean across the entire data ensemble.

A secondary way to obtain the far-field spectral density of the intensity of the pressure fluctuations I is via the Fourier transform of the auto-correlation spectrum of the far-field acoustic pressure in time from Eq. (8) (i.e., via Wiener (1930)'s theorem). Given that for turbulent jets the turbulent statistics are stationary (Morris and Farassat 2002), the spectral density S of the acoustic intensity can be obtained as:

$$S(\boldsymbol{x},\omega) = \frac{1}{32\pi^3\rho_0 c_0^5|\boldsymbol{x}-\boldsymbol{y}|^2}\int_{-\infty}^{+\infty}\int_{V_{y_1}}\int_{V_{y_2}}\frac{\partial^4}{\partial\tau^4} \times \left\langle T_{xx}(\boldsymbol{y}_1,t)T_{xx}(\boldsymbol{y}_2,\tau_0)\right\rangle e^{i\omega\tau}\,d\boldsymbol{y}_1\,d\boldsymbol{y}_2\,d\tau \tag{10}$$

where the time τ_0 is obtained from the far-field approximation $\tau_0 = t + \tau + \hat{\boldsymbol{x}}\cdot\left[\left(\boldsymbol{y}_2-\boldsymbol{y}_1\right)/c_0\right]$, $\hat{\boldsymbol{x}}$ is the direction vector pointing from the observer location, and $\omega = 2\pi\upsilon$ with υ being the signal frequency in Hertz. In the present manuscript, the independent reference systems $\boldsymbol{y}_1$, $\boldsymbol{y}_2$ are based upon the full measurement volume. The definition of the two-point correlation function of the Lighthill's stress tensors in the fixed frame (Lighthill 1952, 1954) can be substituted in the previous equation and computed from the VIC time series, giving the final stationary frame solution for the intensity of the pressure fluctuations:

$$S(\boldsymbol{x},\omega) = \frac{\omega^4}{32\pi^3\rho_0 c_0^5|\boldsymbol{x}-\boldsymbol{y}|^2}\int_{-\infty}^{+\infty}\int_{V_{y_1}}\int_{V_\eta} R_f\left(\boldsymbol{y_1},\boldsymbol{\eta},\tau\right)e^{i\omega\left[\tau-\hat{x}\cdot\frac{\eta}{c_0}\right]}\,d\boldsymbol{y}_1\,d\boldsymbol{\eta}\,d\tau \tag{11}$$

where $R_f\left(\boldsymbol{y_1},\boldsymbol{\eta},\tau\right) = \left\langle T_{xx}(\boldsymbol{y}_1,t)T_{xx}(\boldsymbol{y}_2,t+\tau)\right\rangle$ and $\boldsymbol{\eta} = \boldsymbol{y}_2 - \boldsymbol{y}_1$. One possible advantage of using a moving frame with respect to the turbulence is the relatively easier computation of the convective velocity from the VIC time series, with the local temporal variation of the flow structures. Following the work of Morris and Farassat (2002), by defining a spatial correlation coordinate that accounts for the convection of the eddies with velocity $\boldsymbol{u_c}$:

$$\boldsymbol{\xi} = \boldsymbol{\eta} - \boldsymbol{u_c}\tau \tag{12}$$

it is finally possible to write the Fourier transform of the auto-correlation function of the far-field pressure fluctuations, based upon the two-point cross-correlation function of the Lighthill's stress tensor in the moving frame:

$$S(\boldsymbol{x},\omega) = \frac{\omega^4}{32\pi^3\rho_0 c_0^5|\boldsymbol{x}-\boldsymbol{y}|^2}\int_{-\infty}^{+\infty}\int_{V_{y_1}}\int_{V_\xi} R_m\left(\boldsymbol{y_1},\boldsymbol{\xi},\tau\right)e^{i\omega\left[\tau\left(1-\hat{x}\cdot\frac{\boldsymbol{u_c}}{c_0}\right)-\hat{x}\cdot\frac{\xi}{c_0}\right]}\,d\boldsymbol{y}_1\,d\boldsymbol{\xi}\,d\tau. \tag{13}$$

The local convection velocity of the flow structures is approximated by an iterative filtering procedure as in Schneiders et al. (2014). The previous methodology has been verified to give very similar results to the mean of the time series; however, it has the additional advantage to provide with a more physical convective velocity variation throughout the full time series. Additionally, it can be noted that the term $\left(1-\hat{x}\cdot\frac{\boldsymbol{u_c}}{c_0}\right)$, obtained from the substitution of the variable $\boldsymbol{\eta}$, can be approximated with the convection correction $\left(1-M_c\cos\theta\right)$ with the convective Mach number of the eddies M_c and θ the angle between the convection velocity of the eddies and the observer direction. It has to be noted that from a pure computational time all previous methodologies are relatively similar, when solely starting from discrete time series of tomographic velocity fields. Nevertheless, while Eq. (8) requires all the points of the flow field in time to evaluate the double derivative in time of Lighthill's stress tensor, the formulation in Eqs. (11)–(13) eventually requires only those points where the cross-correlation function is not negligible. This could speed up the evaluation of the acoustic pressure fluctuation for those jet applications where the extent of the source region is limited in the domain. Additional details on all previous derivations can still be found in the study of Morris and Farassat (2002).

4.4 Limitations on resolution and frequency range

A visual flowchart diagram is presented in Fig. 8 to clarify all computational steps. Once verified that the advection model and the spatial resolution are both suitable for the analysis of the flow structures under investigation, a time series of velocity fields can be directly obtained from a single vector field. In particular, as it can be seen from the flowchart, a preliminary time series is propagated to determine the material derivative of the velocity to be used in the VIC+ methodology. The VIC+ methodology constructs a converged divergence-free numerical solution of the experimental vorticity which can be convected accurately for either aerodynamic of aeroacoustic analyses. The presented methodology offers several advantages when studying 3D flows in jets. An important advantage of the technique is the employment of a low repetition system, which typically features cameras having relatively higher pixel density with respect to high-speed ones. Such high-speed cameras, in fact, are typically constrained in the maximum amount of

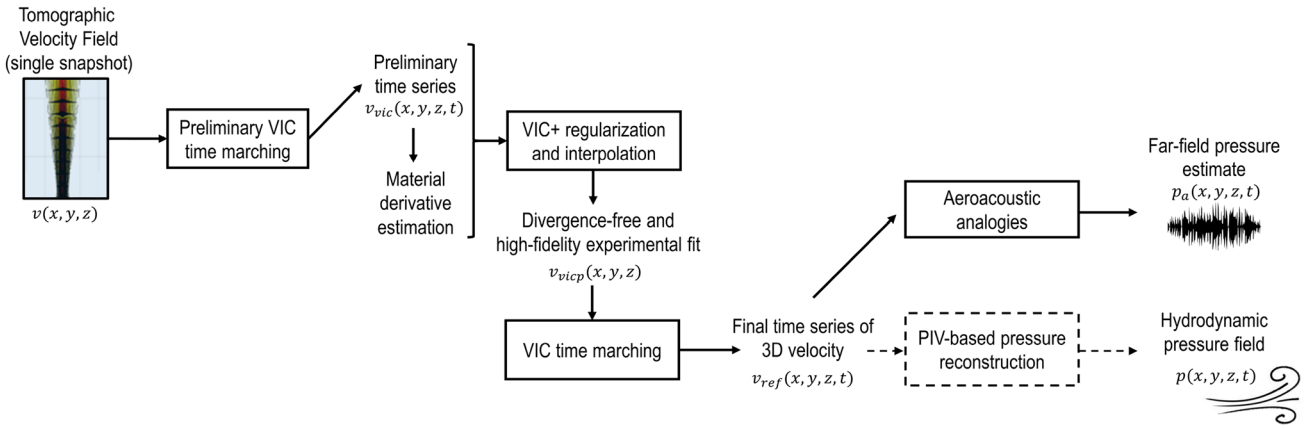

Fig. 8 Flow diagram of the proposed methodology in which each block represents a data processing algorithm

pixel that can be used in the recording per unit of time, especially when requested to reach acquisition frequencies higher than 20 kHz (Scarano 2012). Despite that, limitations in the time-marching algorithm also exist due to the finite spatial resolution and to the limited extension of the jet domain. Specifically, the maximum propagation time of the marching technique is directly proportional to the domain size and inversely proportional to the flow velocity. As indicated by Schneiders et al. (2014), errors in conventional tomographic setups allow to march for a max of about half of a flow pass, also considering that a relatively too long propagation time would lead to the vorticity field exiting the investigated volume. The maximum propagation time determines the length of the time signal of the Lighthill's stress tensor and therefore the lowest frequency of the final far-field acoustic pressure.

The VIC algorithm propagates each single 3D velocity field both forward and backward in time with time steps of 10 μs (set as 70% of the maximum time step to be assigned due to the CFL condition at the specific spatial resolution (Schneiders et al. 2014) for a total time duration of 3 ms. Therefore, the minimum frequency that can be resolved corresponds to half of the total time duration ΔT, i.e., 0.5 kHz. The total time can be translated to a jet marching of about 1/3 of the total domain with a sampling frequency of about 100 kHz. It is worth mentioning that due to the acoustic analogy formulation, the measurement resolution plays an important role in characterizing both the low- and the high-frequency response of the far-field noise spectra. Figure 9 summarizes the limitations of the spatial and temporal resolutions on the far-field acoustic spectrum. A 'true' spectrum is sketched in black, while the ones in blue and red are the equivalent spectra as obtained by the current methodology. That is, the blue one would be obtained by employing a spatial resolution (t.b.n. indicated with a specific spacing h_{res} here for brevity) deemed sufficient to represent the flow

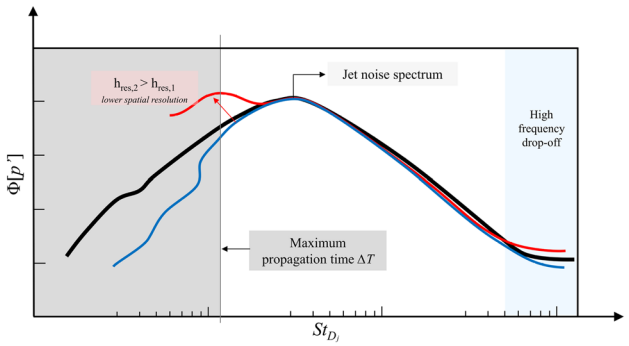

Fig. 9 Effect of spatial resolution and propagation time in the methodology

structures in the field, and a total time propagation ΔT. The red one would be obtained with a relatively lower resolution, but with the same propagation time as used for the blue one. The lowest frequency limit of the methodology is indicated in shaded gray and relates to the maximum propagation time, of the velocity time series, ΔT. At the high-frequency end of the spectrum, the spectrum is affected by the uncertainty in the velocity measurements and is limited by the Nyquist frequency associated with time step *dt*. It must be noted that a sub-optimal resolution would lead to an overestimation of the acoustic energy at low frequency, due to the fact that a relatively larger portion of the resolved turbulence kinetic energy is correlated.

5 Temporal jet evolution by finite vortex-in-cell marching

An instantaneous vector field measured with tomographic PIV is shown in Fig. 10. Contours of constant velocity magnitude (Fig. 10—left) and of constant Q

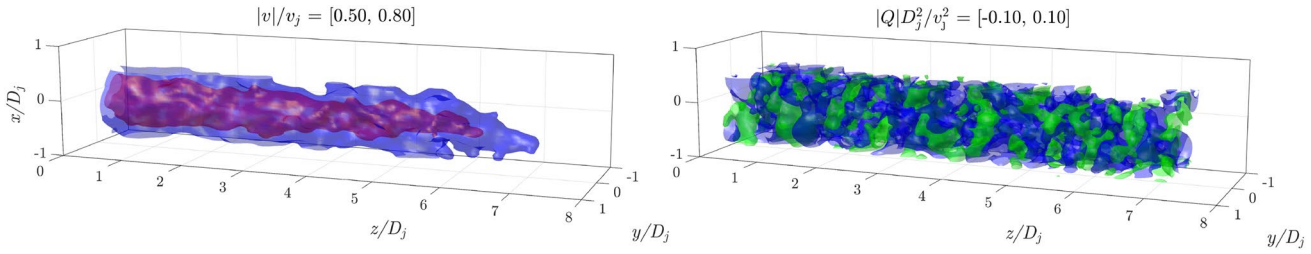

Fig. 10 Instantaneous 3D flow field, left: velocity magnitude, iso-surfaces of velocity magnitude $|v|/v_j$= [0.5, 0.8] in blue/purple, Q-criterion with $Q \cdot D_j^2/v_j^2$= [− 0.10, 0.10] in blue/green

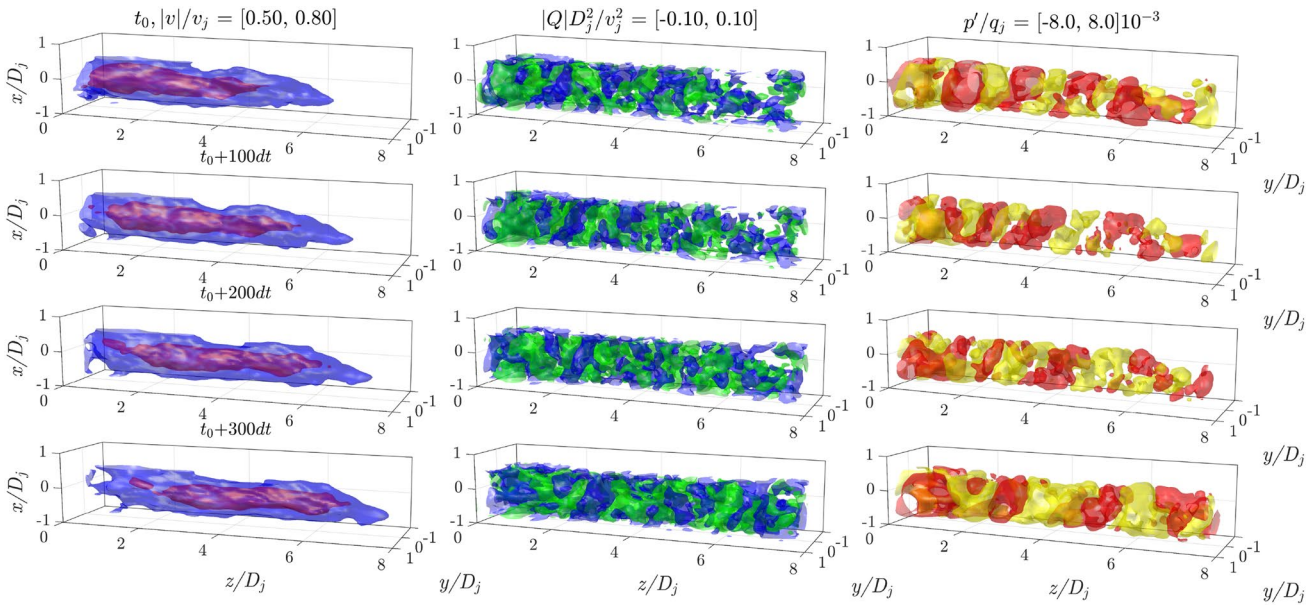

Fig. 11 Time sequence of the jet, left: velocity magnitude, center: Q-criterion, right: pressure fluctuations. Iso-surfaces of velocity magnitude $|v|/v_j$ = [0.5, 0.8] in blue/purple, Q-criterion with $Q \cdot D_j^2/v_j^2$ = [-0.10, 0.10] in blue/green, pressure fluctuations $(p - p_\infty)/q_j = [-8, 8] \cdot 10^{-3}$ in yellow/red, where $q_j = \frac{1}{2}\rho v_j^2$

(Fig. 10—right) are presented. The contours of velocity magnitude $|v|/v_j$ clearly show the turbulent development of the jet consistently with what presented by the stereoscopic and tomographic mean results. Starting from the previous axial location, the high-speed region breaks down into smaller scales, the size of which slowly keeps decreasing as convecting downstream. The same behavior can be better appreciated through Q-criterion visualizations, which present the convection and later breakdown of the turbulent features into finer structures. Moreover, alternating positive and negative Q-criterion contours can be observed throughout the axial development of the jet, additionally associated with a series of circular low- and high-pressure fluctuations moving downstream. Alternating regions in Fig. 10 of high- and low-vortex deformation are well-documented in the literature, and they correspond to the turbulent convection of the 3D ring-like shapes produced by Kelvin-Helmholtz roll-up instabilities, as also reported in (Violato and Scarano 2013).

The 3D evolution of the jet is estimated by applying the vortex-in-cell algorithm to the velocity fields measured with tomographic PIV. Figure 11 shows a few snapshots of the flow field estimated at different time instants through the VIC method. The time separation for visualization purposes is set to a hundred times the propagation time, i.e., 1 ms, with the propagation time being of 10 μs as stated above. Considering that at $M_j = 0.15$ the velocity at the nozzle v_j corresponds to 51 m s^{-1}, the results show displacement of the jet of about $1D_j$ per 100 time steps, from $t = t_0$ to $t = t_0 + 300\ dt$ in Fig. 11. The effect of the convection is visible by the Q-criterion, indicated by the coherent propagation of the flow structures, shown in Fig. 11—center, stretching until reaching the end of the domain. Figure 11—right shows also the pressure fluctuations of the jet estimated from the

time-resolved velocity field. The pressure field is observed to follow the same structure topology as indicated by the Q-contours in Fig. 11—center in the entire domain. This concept is better visualized in the 2D visualizations in the middle of the jet of Fig. 12, which show a frame of velocity magnitude, Q-, and pressure fluctuations contours. In particular, several regions in the axial direction with alternating sign recall the vorticity structures extending azimuthally that are caused by Kelvin–Helmholtz roll-up instabilities (Violato et al. 2011). For axial locations further than $z/D_j = 4$ to 6, the pairing process of two consecutive structures de-correlates the pressure fluctuations with respect to the Q-contours. In addition, it can be noted that the length scales of the pressure fluctuations are about double that of the associated Q-structures, consistent with what reported by Ghaemi et al. (2012).

6 Far-field pressure spectra evaluation

The evaluation of the acoustic pressure fluctuations in the far field is performed using VIC time series as input. As explained in Sect. 4, the final data from the VIC time series are used as input for three integral formulations based upon Lighthill's aeroacoustic analogy. First, a validation step is carried out by comparing the reference microphone data with both experimental results and analytical models from the literature. For consistency, all plotted results are converted into spectral density of acoustic pressure fluctuations, derived or plotted at a microphone angle of 90 degrees from the jet axis and scaled to the same distance of 1 m. In particular, from the study of Morris and Farassat (2002) the model from Tam and Aurialt (1999) is taken in its original form (TA) and in the modified one (TAMF), with the referenced results from Tanna et al. (1976) in the form of far-field acoustic pressure. The main difference between the original (TA) and the modified version (TAMF) is an "a-posteriori" fitting of the empirical coefficients to the experimental data (Morris and Farassat 2002). In Fig. 13, the experimental data from this study are plotted together with the previously mentioned empirical models and experimental data from Tanna et al. (1976). Figure 13 is plotted from a Strouhal number of 0.3, corresponding to a frequency of about 300 Hz in the limit of the anechoic facility. However, as indicated by Morris and Farassat (2002), recently developed empirical models correctly predict the spectrum of pressure fluctuations up to a $St_{D_j} \approx 1$, while a more pronounced sensitivity to the empirical coefficients is found for a $St_{D_j} > 1$ range. In this respect, the formulation of Tam and Aurialt (1999) has been found to better predict the far-field pressure spectra with respect to the original form from Lighthill (Lighthill 1952, 1954). As indicated by Morris and Farassat (2002), the main assumption that from Eq. (8) is carried out to build up the empirical model based upon Lighthill's original form is the compactness of the source. This assumption is needed to simplify the formulation and obtain a predicting model based upon a few experimental coefficients. The revised version obtained by

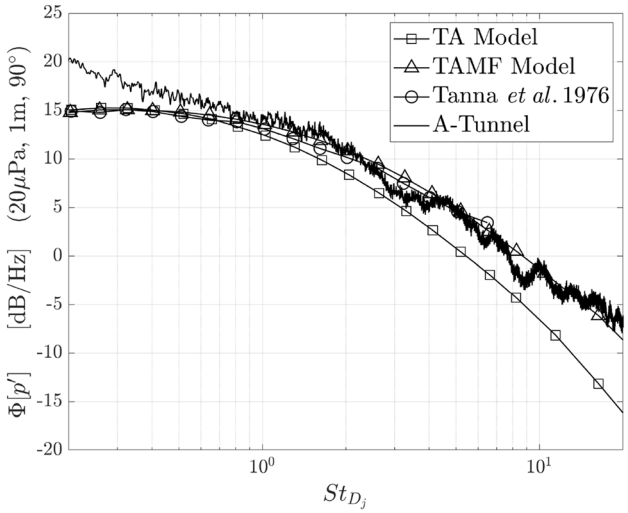

Fig. 13 Spectral density of the acoustic pressure fluctuations at 90° from the jet axis. All results are scaled to the case of $M_j = 0.15$, temperature ratio $T_j/T_\infty = 1$ and far-field location $r/D_j = 20$: microphone results from this study (A-tunnel), experimental results from Tanna et al. (1976), prediction values from Tam and Aurialt (1999) original model (TA), and with empirical coefficient modified to the experimental data as in Morris and Farassat (2002) (TAMF)

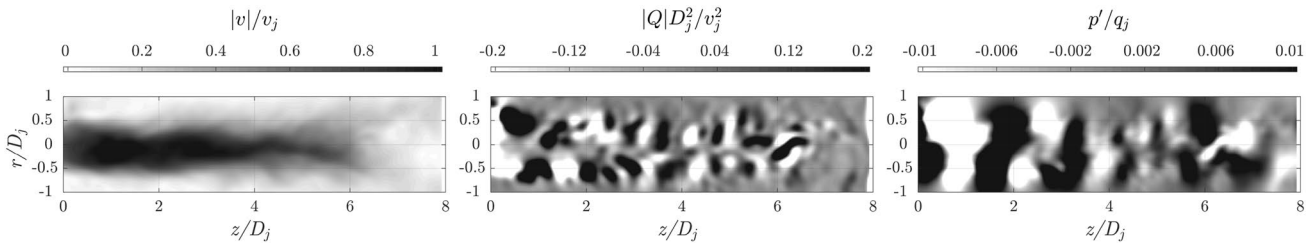

Fig. 12 Two-dimensional detail of the spatial organization of the flow structures; (left) velocity magnitude, (center) Q-criterion, (right) pressure fluctuations

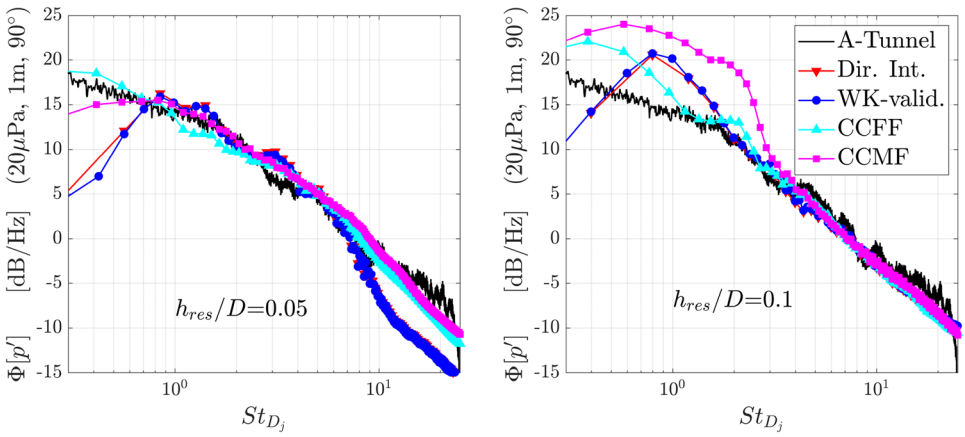

Fig. 14 Spectral density of the pressure fluctuations at 90° from the jet axis, comparison for the jet with $M_j = 0.15$, scaled to $r/D_j = 20$, temperature ratio $T_j/T_\infty = 1$: microphone results from this study (A-tunnel), direct integration from Eq. (8) (Dir. Int.), validation of the previous approach via the Wiener–Khinchin theorem (Wiener 1930) (WK-valid.), two-point cross-correlation formulation in the fixed frame by Eq. (11) (CCFF), moving formulation from Eq. (13) (CCMF)

Tam and Aurialt (1999) does not entail such assumption, and it is more physically adherent to the generation of pressure fluctuations from small-scale turbulence, since proportional to the local turbulent kinetic energy per unit volume. The spectrum from the direct microphone measurement confirms the previous observations, agreeing from $St_{D_j} \approx 0.5$ to both the measurements of Tanna et al. (1976) and to the empirical model of Tam and Aurialt (1999), with coefficients adapted from the experimental data. It has to be noted that the original formulation without tuned coefficients performs fairly well already, with relatively lower constructive contribution to the far-field noise of the fine-scale turbulence at $St_{D_j} > 1$. This is most probably due to the choice of the original coefficients as explained by Morris and Farassat (2002).

The original aeroacoustic analogy as derived from Lighthill or Lilley can still be used in its original form just before making assumptions for its simplification, with the aim to estimate the acoustic far-field pressure fluctuations in function of the velocity distribution obtained from the vortex-in-cell methodology. A detailed analysis of the capabilities of the methodology to correctly represent the spatial organization and evolution of coherent flow structures can be found in Schneiders et al. (2016, 2018), and very recently in Fiscaletti et al. (2022). The advantages of the combination of the time-marching methodology with the integral form of the far-field pressure lie behind the possibility to use uncorrelated tomographic velocity fields, thus saving on the costs associated with a high-speed tomographic system. In Fig. 14, the three different formulations as presented in Sect. 4 are reported for the far-field pressure estimate according to Eqs. (8), (11), and (13). In particular, the volume integration via the Green's function solution of Eq. (8) (indicated with Dir. Int.) is compared to the formulations employing the two-point cross-correlation of the Lighthill's stress sensor. For the latter, the fixed-frame formulation in Eq. (11) is referred to as CCFF in the plot, while the moving formulation in Eq. (13) is referred to as CCMF. Additionally, a further step is carried out to verify the correctness of the integration procedure, by comparing the auto-spectral density of the pressure fluctuations with the Fourier transform of the auto-correlation function of the pressure. As from the Wiener–Khinchin theorem (Wiener 1930), i.e., VK-valid in Fig. 14, it can be seen that the results coincide within numerical errors with the integral solution of Eq. (8) (Dir. Int.). Consistent with Figs. 13, 14 shows the spectral density of the far-field acoustic pressure at a corrected listener position at 90° azimuthal angle relative to the jet axis, at a radial distance of $r = 20D_j$. Data are averaged over 400 out of the 500 total uncorrelated amount of samples. Convergence of the spectra within 2 dB from the solutions of Fig. 14 is obtained already with about 150 independent time series in the range of the plotted Strouhal numbers.

As explained in the previous sections, the longest time series is achieved by running the VIC for a duration of $\sim 2.5D_j/U_j$, i.e., corresponding to about $\pm$ 1/3 of the overall flow field. For the $M_j = 0.15$ case, the lowest frequency at which data can be reliably computed corresponds to $St_{D_j} \approx 1$. Very few differences can be appreciated between the different formulations, mainly in the way the low-frequency regime is treated. In particular, minor discrepancies can be found by using either the fixed-frame or the moving-frame formulation, given that the two-point correlation is still obtained from the Lighthill's stress tensor. Although both two-point correlation methods show very similar results to the original integral formulation, the two methodologies are expected to be more reliable with noisy data or with very large domains, given that the two-point correlation of uncorrelated flow structures that are affected by noise is expected to lead to negligible contributions. In the integral formulation, on the other hand, the measurement noise sums up and ultimately produces an overestimation of the far-field noise.

A final investigation is carried out to clarify the effect of a lowered spatial resolution on the noise estimation. The analysis is conducted by sub-sampling the

three-dimensional velocity vector fields, which leads to obtain a larger grid spacing in the data. In Fig. 14, the effects of halving the spatial resolution on the estimated pressure spectra are assessed. The response decay at high frequency is still relatively robust, and it appears to be rather insensitive to the spatial resolution as far as the formulations based on cross-correlation are concerned. On the other hand, the effect of reducing the spatial resolution is strong at low frequency, and it produces an overestimation of the calculated noise from all formulations, in a Strouhal number range between 1 and 2. This illustrates what is discussed alongside Fig. 9, namely that the overestimation is caused by a prominent constructive interference from unresolved and relatively larger flow structures.

7 Conclusions

This study presents a methodology to compute the relatively high-frequency response of the spectral density of the far-field pressure fluctuations of a jet from uncorrelated tomographic PIV vector fields. The technique is applied to a turbulent subsonic jet at three different Mach numbers, and data are presented for the intermediate one $M_j = 0.15$. The methodology combines the vortex-in-cell method, used to extract a time series from a single-frame tomographic PIV velocity field, with different integral formulation of the Lighthill's equation, to obtain an estimate of the far-field acoustic pressure fluctuations. The technique has the potential of overcoming the limitations of the previous empirical models used for prediction of the high-frequency jet noise spectral distribution, which is known to be sensitive to the choice of fitting coefficient. In order to evaluate the quality of both the velocity and the far-field pressure fluctuations, the results are compared with those from previous literature and with pressure spectra obtained from acoustic measurements. The collapse of the data is deemed reliable from a Strouhal number of 1 based upon the jet diameter and on the max propagation time reached with the vortex-in-cell contribution. A brief investigation on the effects of halving the resolution confirms that the relatively high-frequency spectral decay due to the convection of the resolved flow structures can be captured, although suffering from an overestimation of the constructive effects at relatively lower frequency.

Acknowledgements The authors would like to acknowledge Leandro Falcão Rego and Gabriel Gonzalez Saiz for their help with the experimental setup and with the data processing. D.F. is funded by the Marie Skłodowska–Curie Actions of the European Union's Horizon 2020 Program under the Grant Agreement No. 895478-ANACLETO.

References

Adrian RJ, Yao CS (1985) Pulsed laser technique application to liquid and gaseous flows and the scattering power of seed materials. Appl Opt 24(1):44

Aleyasin SS, Tachie MF, Koupriyanov M (2017) PIV measurements in the near and intermediate field regions of jets issuing from eight different nozzle geometries. Flow Turbul Combust 99(2):329–351

Anderson ABC (1956) Vortex-ring structure-transition in a jet emitting discrete acoustic frequencies. J Acoust Soc Am 28(5):914–921

Baars WJ, Murray NE, Tinney CE (2021) A proper framework for studying noise from jets with non-compact sources. J Fluid Mech 929:A23

Bastin F, Lafon P, Candel S (1997) Computation of jet mixing noise due to coherent structures: the plane jet case. J Fluid Mech 335:261–304

Bernal PL, Roshko A (1986) Streamwise vortex structure in plane mixing layers. J Fluid Mech 170(1):499–525

Bogey C, Bailly C (2007) An analysis of the correlations between the turbulent flow and the sound pressure fields of subsonic jets. J Fluid Mech 583:71–97

Bogey C, Bailly C, Juvé D (2003) Noise investigation of a high subsonic, moderate reynolds number jet using a compressible les. Theor Comput Fluid Dyn 16(4):273–297

Boillot A, Prasad AK (1996) Optimization procedure for pulse separation in cross-correlation PIV. Exp Fluids 21(2):87–93

Breaky DES, Jordan P, Cavalieri AVG, Nogueira P, Léon O, Colonius T, Rodrìguez D (2017) Experimental study of turbulent-jet wave packets and their acoustic efficiency. Phys Rev Fluids 2:124601

Bruun HH (1995) Hot wire anemometry: principles and signal analysis. Oxford University Press, Oxford

Cavalieri AVG, Jordan P, Colonius T, Gervais Y (2012) Axisymmetric superdirectivity in subsonic jets. J Fluid Mech 704:388–420

Charonko JJ, King CV, Smith BL, Vlachos PP (2010) Assessment of pressure field calculations from particle image velocimetry measurements. Meas Sci Technol 21(10):105401

Christiansen IP (1973) Numerical simulation of hydrodynamics by the method of point vortices. J Comput Phys 13(3):363–379

Citriniti J, George WK (2000) Reconstruction of the global velocity field in the axisymmetric mixing layer utilizing the proper orthogonal decomposition. J Fluid Mech 418(137):137–166

Colonius T, Lele SK, Moin P (1997) Sound generation in a mixing layer. J Fluid Mech 330:375–409

Courant R, Friedrichs K, Lewy H (1928) Über die partiellen differenzengleichungen der mathematischen physik. Math Ann 100(1):32–74

Crow SC, Champagne FH (1971) Orderly structure in jet turbulence. J Fluid Mech 43:547–591

de Kat R, van Oudheusden BW (2012) Instantaneous planar pressure determination from PIV in turbulent flow. Exp Fluids 52(5):1089–1106

Elsinga GE, Scarano F, Wieneke B, van Oudheusden BW (2006) Tomographic particle imagee velocimetry. Exp Fluids 41:933–947
Fiscaletti D, Ragni D, Overmars FJ, Westerweel J, Elsinga E (2022) Tomographic long-distance μPIV to investigate the small scales of turbulence in a jet at high Reynolds number. Exp Fluids 63(9):1–6
Freund JB (2001) Noise sources in a low-Reynolds-number turbulent jet at Mach 0.9. J Fluid Mech 438:277–305
Fu Z, Agarwal A, Cavalieri AVG, Jordan P, Brès GA (2017) Turbulent jet noise in the absence of coherent structures. Phys Rev Fluids 2(6):064601
Ghaemi S, Ragni D, Scarano F (2012) PIV-based pressure fluctuations in the turbulent boundary layer. Exp Fluids 53(6):1823–1840
Glauser MN, George WK (1987) Orthogonal decomposition of the axisymmetric jet mixing layer including azimuthal dependence. Advances in turbulence. Springer, Berlin, Heidelberg, pp 357–366
Goldstein ME (1976) Aeroacoustics. McGraw-Hill, New York
Guj G, Carley M, Camussi R, Ragni A (2003) Acoustic identification of coherent structures in a turbulent jet. J Sound Vib 259(5):1037–1065
Herman GT, Lent A (1976) Iterative reconstruction algorithms. Comput Biol Med 6:273–294
Hewitt RE, Duck PW (2011) Pulsatile jets. J Fluid Mech 670:240–259
Hussain F (1986) Coherent structures and turbulence. J Fluid Mech 173:303–356
Hussein HJ, Capp SP, George WK (1994) Velocity measurements in a high-Reynolds-number momentum-conserving, axisymmetric, turbulent jet. J Fluid Mech 258(31):31–75
Iqbal M, Thomas F (2007) Coherent structure in a turbulent jet via a vector implementation of the proper orthogonal decomposition. J Fluid Mech 571(281):281–326
Jaunet V, Jordan P, Cavalieri AVG (2017) Two-point coherence of wave packets in turbulent jets. Phys Rev Fluids 2:024604
Jeong J, Hussain F (1995) On the identification of a vortex. J Fluid Mech 285:69–94
Jordan P, Colonius T (2013) Wave packets and turbulent jet noise. Ann Rev Fluid Mech 45:173–195
Jordan P, Schlegel M, Noack BR, Tinney CE (2007) Identifying noisy and quiet modes in a jet. AIAA Pap 2007-3602 16(4):273–297
Jung D, Gamard SG, George WK (2004) Downstream evolution of the most energetic modes in a turbulent axisymmetric jet at high Reynolds number. Part 1. the near-field region. J Fluid Mech 514(205):173–204
Kaushik M, Kumar R, Humrutha G (2015) Review of computational fluid dynamics studies on jets. Am J Fluid Dyn 5:1–11
Kerhervé F, Jordan P, Gervais Y, Valiere J, Braud P (2004) Two-point laser doppler velocimetry measurements in a Mach 1.2 cold supersonic jet for statistical aeroacoustic source model. Exp Fluids 37:419–437
Kerhervé F, Jordan P, Cavalieri AVG, Delville J, Bogey C, Juvé D (2012) Educing the source mechanism associated with downstream radiation in subsonic jets. J Fluid Mech 710:606–640
Ko NWM, Davies POAL (1971) The near field within the potential cone of subsonic cold jets. J Fluid Mech 50:49–78
Koumoutsakos P (2005) Multiscale flow simulations using particles. Ann Rev Fluid Mech 37:457–487
Kyle DM, Sreenivasan KR (1993) The instability and breakdown of a round variable-density jet. J Fluid Mech 249:619–664
Lasagna D, Buxton ORH, Fiscaletti D (2021) Near-field coherent structures in circular and fractal orifice jets. Phys Rev Fluids 6:044612
Lew PT, Mongeau L (2010) Noise prediction of a subsonic turbulent round jet using the lattice-boltzmann method. J Acoust Soc Am 128(3):1118–1127
Liepmann D, Gharib M (1992) The role of streamwise vorticity in the near field entrainment of round jets. J Fluid Mech 245:643–668
Lighthill MJ (1952) On sound generated aerodynamically. I. General theory. Proc R Soc A 211(1107):564–587
Lighthill MJ (1954) On sound generated aerodynamically. II. Turbulence as a source of sound. Proc R Soc A 222(1148):1–32
Lilley GM (1974) On the noise from jets. Noise mechanisms. CP-131 AGARD, pp 13.1–13.12
List EJ (1982) Turbulent jets and plumes. Ann Rev Fluid Mech 14:189–212
Mankbadi R, Liu JTC (1984) Sound generated aerodynamically revisited: large-scale structures in a turbulent jet as a source of sound. Phil Trans R Soc Lond A 311(1516):183–217
Martin JE, Meiburg E (1991) Numerical investigation of three-dimensionally evolving jets subject to axisymmetric and azimuthal perturbations. J Fluid Mech 230:271–318
Matsuda T, Sakakibara J (2005) On the vortical structure in a round jet. Phys Fluids 17:025106
Merino-Martinez R, Rubio Carpio A, Lima Pereira TL, van Herk S, Avallone F, Ragni D, Kotsonis M (2020) Aeroacoustic design and characterization of the 3d-printed, open-jet, anechoic wind tunnel of delft university of technology. Appl Acoust 170:107504
Morris PJ (2009) A note on noise generation by large scale turbulent structures in subsonic and supersonic jets. Intl J Aeroacoustics 8(4):301–316
Morris PJ, Farassat F (2002) Acoustic analogy and alternative theories for jet noise prediction. AIAA J 40(4):671–680
Nogueira PAS, Cavalieri AVG, Jordan P, Jaunet V (2019) Large-scale streaky structures in turbulent jets. J Fluid Mech 873(211):211–237
Papamoschou D (2011) Wavepacket modeling of the jet noise source. AIAA Pap 2011–2835
Pinier JT, Glauser M (2017) Dual-time piv investigation of the sound producing region of the high-speed jet. AIAA Pap 2007–3857
Pröbsting S, Scarano F, Bernardini M, Pirozzoli S (2013) On the estimation of wall pressure coherence using time-resolved tomographic PIV. Exp Fluids 54(7):1–15
Raffel M, Willert CE, Wereley S, Kompenhans J (2007) Particle image velocimetry - a practical guide. Springer-Verlag, Berlin, Heidelberg
Ragni D, Ashok A, van Oudheusden BW, Scarano F (2009) Surface pressure and aerodynamic loads determination of a transonic airfoil based on particle image velocimetry. Meas Sci Technol 20:074005
Samie M, Lavoie P, Pollard A (2021) Quantifying eddy structures and very-large-scale motions in turbulent round jets. J Fluid Mech 916(A2)
Sandham ND, Morfey CL, Hu Z (2006) Sound radiation from exponentially growing and decaying surface waves. J Sound Vib 294:355–361
Scarano F (2012) Tomographic PIV: principles and practice. Meas Sci Technol 24(1):012001
Scarano F, Moore P (2012) An advection-based model to increase the temporal resolution of PIV time series. Exp Fluids 52(4):919–933
Scarano F, Riethmuller ML (1999) Iterative multigrid approach in PIV image processing with discrete window offset. Exp Fluids 26(6):513–523
Schneiders JFG, Dwight RP, Scarano F (2014) Time-supersampling of 3d-PIV measurements with vortex-in-cell simulation. Exp Fluids 55(3):1–15
Schneiders JFG, Pröbsting S, Dwight R, van Oudheusden BW, Scarano F (2016) Pressure estimation from single-snapshot tomographic PIV in a turbulent boundary layer. Exp Fluids 57(53):1–14
Schneiders JFG, Avallone F, Pröbsting S, Ragni D, Scarano F (2018) Pressure spectra from single-snapshot tomographic PIV. Exp Fluids 59(57):1–15

Schram C, Hirschberg A (2003) Application of vortex sound theory to vortex pairing noise: sensitivity to errors in flow data. J Sound Vib 266:1079–1098

Schram C, Taubitz S, Anthoine J, Hirschberg A (2005) Theoretical/empirical prediction and measurement of the sound produced by vortex pairing in a low Mach number jet. J Sound Vib 281:171–187

Schrijer FFJ, Scarano F (2014) Effect of predictor-corrector filtering on the stability and spatial resolution of iterative PIV interrogation. Exp Fluids 45(5):927–941

Seiner JM, Ukeiley L, Ponton MK (1999) Jet noise source measurements using PIV. In: 5th AIAA/CEAS aeroacoustics conference and exhibit, Bellevue, WA, AIAA Paper. pp 99–1869

Suponitsky V, Sandham ND, Morfey CL (2010) Linear and nonlinear mechanisms of sound radiation by instability waves in subsonic jets. J Fluid Mech 658:509–538

Suzuki T (2010) A review of diagnostic studies on jet-noise sources and generation mechanisms of subsonically convecting jets. Fluid Dyn Res 42(1):014001

Tam CKW, Aurialt L (1999) Jet mixing noise from fine-scale turbulence. AIAA J 37(2):145–153

Tanna HK, Dean PD, Burrin RH (1976) The generation and radiation of supersonic jet noise, vol 3. Turbulent mixing noise data. Tech. Rep. AFAPL-TR-76-65-Vol.3, US Airforce Propulsion Laboratory

Taylor GI (1938) The spectrum of turbulence. Proc R Soc Lond 164(919):476–490

Tinney CE, Ukeiley LS, Glauser MN (2008) Low-dimensional characteristics of a transonic jet. Part 2. Estimate and far-field prediction. J Fluid Mech 615:53–92

van Oudheusden BW (2013) PIV-based pressure measurement. Meas Sci Technol 24:032001

Violato D, Scarano F (2011) Three-dimensional evolution of flow structures in transitional circular and chevron jets. Phys Fluids 23:124104

Violato D, Scarano F (2013) Three-dimensional vortex analysis and aeroacoustic source characterization of jet core breakdown. Phys Fluids 25(1):015112

Violato D, Moore P, Scarano F (2011) Lagrangian and eulerian pressure field evaluation of rod-airfoil flow from time-resolved tomographic PIV. Exp Fluids 50(4):1057–1070

Westerweel J (1994) Efficient detection of spurious vectors in particle image velocimetry data. Exp Fluids 16(3–4):236–247

Westerweel J (1997) Fundamentals of digital particle image velocimetry. Meas Sci Technol 8(12):1379–1392

Wieneke B (2015) PIV uncertainty quantification from correlation statistics. Meas Sci Technol 26(7):0744002

Wiener N (1930) Generalized harmonic analysis. Acta Math 55:117–258

Yule AJ (1978) Large structure in the mixing layer of a round jet. J Fluid Mech 89:413–432